PROCEEDINGS A

royalsocietypublishing.org/journal/rspa

Research

Cite this article: Benham GP. 2023 Anisotropy distorts the spreading of a fixed volume porous gravity current. *Proc. R. Soc. A* **479**: 20230271. https://doi.org/10.1098/rspa.2023.0271

Received: 25 April 2023
Accepted: 18 October 2023

Subject Areas:
environmental engineering, applied mathematics, fluid mechanics

Keywords:
gravity currents, porous media, anisotropy

Author for correspondence:
Graham P. Benham
e-mail: graham.benham@ucd.ie

Electronic supplementary material is available online at https://doi.org/10.6084/m9.figshare.c.6922121.

THE ROYAL SOCIETY PUBLISHING

Anisotropy distorts the spreading of a fixed volume porous gravity current

Graham P. Benham

School of Mathematics and Statistics, University College Dublin, Belfield, Dublin 4, D04 V1W8, Ireland

GPB, 0000-0003-1664-6976

We consider the release and subsequent gravity-driven spreading of a dense finite volume of fluid in an anisotropic porous medium bounded by an impermeable substrate. When the permeability in the vertical direction is much smaller than in the horizontal direction, as is the case in many real geological reservoirs, this restricts the spread of the current to a very thin layer near the impermeable base. Using a combination of asymptotic analysis and finite difference computations of Darcy flow, we show that there exist two distinct flow regimes. At early times, the bulk of the current descends slowly and uniformly, injecting fluid into thin finger-like regions near the base. At much later times, the current transitions to the classical gravity-driven solution and continues to spread with a self-similar shape. One interesting consequence is that the swept volume of the current grows differently depending on the anisotropy of the medium. This has important consequences for managing contaminant spills, where it is important to minimize the contacted volume of the aquifer, or during geological CO_2 sequestration where a larger contacted volume results in more CO_2 being stored.

1. Introduction

Gravity-driven flows resulting from the release of a fluid within a porous medium are a common feature of environmental fluid dynamics. For example, such flows arise when groundwater responds to heavy rainfall [1], after the spillage of a contaminant [2], or during the geological storage of carbon dioxide in saline aquifers [3]. Since all geological aquifers are heterogeneous and

often this heterogeneity manifests as an anisotropic permeability field [4], it is important to quantify how this affects the migration speeds and shape of the current. This is particularly relevant to situations where it is desirable to minimize the volume of the aquifer contacted by the fluid (e.g. containing the spread of a contaminant) or to maximize the contacted volume (e.g. trapping residual saturation during CO_2 storage).

In the case of homogeneous and isotropic porous media, there have been numerous studies on the evolution of fixed volume gravity currents. Some of these studies have treated single-phase flows [5], while others have incorporated multi-phase effects such as residual trapping [6,7] and dissolution within the ambient fluid [8]. In some cases, simple scaling laws were derived by exploiting the self-similar properties of gravity currents, as shown by [9] in the case of single-phase flow, and by [10] in the case of trapped residual saturation. Later work by [11–13] explored the transition to self-similarity in both confined and unconfined settings. However, less attention has been paid to the case of heterogeneous or anisotropic porous media, despite the relevance to real geological reservoirs.

Nevertheless, some progress has been made for specific types of buoyancy-driven flows in heterogeneous media. For example, several studies have investigated how anisotropy affects convective dissolution within an ambient fluid phase [14–16]. In the case of gravity currents resulting from constant injection, [17] explored how heterogeneities of different lateral and vertical scales affect the migration speed of a CO_2 plume. Likewise, [18] addressed the case of a gravity current resulting from point source injection in an anisotropic medium. In this study, it was shown that anisotropy can cause a build-up of pressure that stretches the flow into an ellipsoid shape during an early-time regime of the flow, before transitioning to a gravity-dominated regime at much later times. However, no studies have addressed how heterogeneity affects the spreading of a released volume of fluid (i.e. in the absence of injection), despite the relevance to post-injection scenarios during CO_2 storage, and to post-leakage scenarios in the context of contaminant spills.

CO_2 storage in geological reservoirs is one of the key proposed technologies to reduce emissions and limit the effects of global warming [3]. In such scenarios, buoyant CO_2 is injected into a brine-filled reservoir beneath an impermeable cap rock. Once the injection is switched off, the CO_2 rises and spreads out beneath the cap rock, with a fraction of its mass being lost to residual trapping (via the drainage/imbibition cycle) and dissolution within the surrounding brine [8,19]. Hence, to quantify the trapping potential of different geological reservoirs (e.g. when choosing potential storage sites), it is important to understand how the anisotropy of the aquifer may affect the historical migration of the current across the pore space. In the context of a contaminant spillage, the objective is to contain and minimize the spread of a harmful fluid within an aquifer. Therefore, in a similar manner to the CO_2 storage problem, it is necessary to quantify how and where the contaminant fluid will spread in response to the heterogeneity of the aquifer, once the leak has been closed off [20].

In this study, we demonstrate that anisotropy restricts the flow of the gravity current to thin finger-like regions spreading near the impermeable boundary, qualitatively similar to those predicted by other studies [17]. Due to this flow distortion, the swept volume of the current is reduced for anisotropic aquifers. This indicates that isotropic aquifers may have better potential for certain forms of CO_2 trapping that depend on the contacted volume of pore space. By contrast, in the case of a contaminant spill, anisotropic aquifers may help contain the spread of the fluid by restricting the flow to a reduced fraction of the porous medium.

2. Finite release in two-dimensional anisotropic media

(a) Release and subsequent dynamics

We consider an anisotropic porous medium in which the horizontal permeability k_H is much larger than the vertical permeability k_V. Such anisotropic flow properties are a common feature

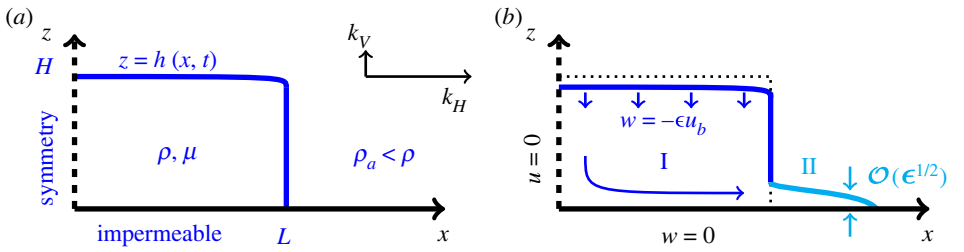

Figure 1. Schematic diagram. (*a*) A finite volume $2LH\phi$ of dense fluid is released into a porous medium with an anisotropic permeability field $k_H \gg k_V$ above an impermeable base. (*b*) The medium is initially saturated with a less dense fluid so that the bulk region (I) descends slowly at speed $-\epsilon u_b$, where $\epsilon = k_V/k_H$ and u_b is the buoyancy velocity (2.10), while a thin finger region (II) develops near the base of the current. Note that the aspect ratio $\alpha = H/L$ could be either small or large depending on the application (see later discussion in §6).

in geological reservoirs and may result from the deposition of successive layers of fine and coarse material or from post-depositional compaction of the formation [21]. As we will show, the anisotropy of the medium restricts the vertical flow of the bulk of the fluid, which we denote region I (figure 1), resulting in a slow migration towards the impermeable boundary. Meanwhile, gravity-driven spreading is limited to thin finger-like regions near the base, which we denote region II.

To start with we restrict our attention to two-dimensional flows (although radially symmetric flows will be addressed later in §5) and we consider the release of a volume (per unit width) of fluid with constant density ρ. The surrounding porous medium is initially saturated with an ambient fluid with relatively smaller density $\rho_a < \rho$. Due to the Boussinesq approximation [22], these results also apply in the case of a lighter fluid (e.g. CO_2) released within a porous medium saturated with a heavier fluid (e.g. brine), with the impermeable boundary located above rather than below.

We take the viscosity of the released fluid[1] to be μ, and we consider that the initial shape is rectangular, with dimensions $2L \times H$. It should be noted, however, that these results would apply to any similar convex shape, as shown in figure 8 and discussed in more detail in appendix A.

The flow in the released volume of fluid is subject to the two-dimensional Darcy equations,

$$\mathbf{u} = -\frac{1}{\mu}\underline{\underline{\mathbf{k}}} \cdot \nabla[p + \rho g z] \tag{2.1}$$

and

$$\nabla \cdot \mathbf{u} = 0, \tag{2.2}$$

where $\mathbf{u}$ is the Darcy velocity vector, p is the pressure and $\underline{\underline{\mathbf{k}}} = \mathrm{diag}(k_H, k_V)$ is the anisotropic permeability field in the x, z directions. Combining (2.1) and (2.2), the pressure satisfies Laplace's equation with anisotropic coefficients,

$$\frac{\partial^2 p}{\partial x^2} + \epsilon \frac{\partial^2 p}{\partial z^2} = 0, \tag{2.3}$$

where the anisotropy is given by

$$\epsilon = \frac{k_V}{k_H} \ll 1. \tag{2.4}$$

The boundary conditions for the flow in region I are as follows. The left hand and bottom boundaries, $x = 0$, $z = 0$, are assumed to be symmetric and impermeable, respectively, so we

[1]The viscosity of the ambient fluid is not relevant here since the domain is infinitely deep, as discussed in [23].

royalsocietypublishing.org/journal/rspa Proc. R. Soc. A 479: 20230271

prescribe no normal flow,

$$u = 0: \quad x = 0 \tag{2.5}$$

and

$$w = 0: \quad z = 0. \tag{2.6}$$

Likewise, at the fluid interface, which we denote $z = h(x, t)$, we impose the dynamic and kinematic boundary conditions

$$p = p_a - \rho_a g h: \quad z = h(x, t) \tag{2.7}$$

and

$$w = \phi \frac{\partial h}{\partial t} + u \frac{\partial h}{\partial x}: \quad z = h(x, t). \tag{2.8}$$

The former condition matches the pressure in the fluid with the ambient hydrostatic pressure (note that the reference pressure p_a is the ambient value at $z = 0$), while the latter condition imposes that a particle at the interface remains at the interface [24,25].

In the limit $\epsilon \to 0$, mass conservation (2.2) indicates that if there is no vertical flow (i.e. $k_V = 0$) then there cannot be any horizontal flow either. Essentially, the governing equation (2.3) implies that the pressure (which is continuous) is set by the ambient fluid, such that $p = p_a - \rho_a g z$, and the resulting velocities are $u = w = 0$. Hence, the interface remains at the initial position $z = h_0(x)$ for all time.

Now let us consider the case of a strongly anisotropic porous medium, such that $0 < \epsilon \ll 1$. In this case, the solution can be found by performing an asymptotic expansion of the pressure in powers of ϵ. Within this expansion, the leading order contribution to the pressure is simply the solution to the isotropic problem (i.e. with $\epsilon = 0$ exactly). Hence, for the same reasons as described above, the leading order pressure is hydrostatic and set by the ambient fluid, $p = p_a - \rho_a g z$. However, by inserting this pressure into Darcy's Law (2.1), we now derive a small but finite (i.e. first order) vertical velocity within region I, such that

$$w = -\epsilon u_b, \tag{2.9}$$

where

$$u_b = \frac{k_H \Delta \rho g}{\mu}, \tag{2.10}$$

is the buoyancy velocity and $\Delta \rho = \rho - \rho_a$. Since (2.9) does not satisfy the impermeability condition (2.6), it is necessary to re-evaluate the solution near $z \approx 0$ using boundary layer theory.

Mathematically speaking, (2.3) is a singular perturbation problem since it is a second-order partial differential equation (PDE) with a small parameter in front of a second derivative. This indicates that not all vertical boundary conditions can be satisfied by the leading order solution. Specifically, the dynamic boundary condition (2.7) is imposed at $z = h$ to ensure continuity of pressure, while the impermeability condition (2.6) at $z = 0$ is left unsatisfied. To correct this requires rescaling the solution to investigate changes over a small vertical distance near $z \approx 0$, also known as a boundary layer. By inspection of (2.3), it is clear that z must be rescaled by a factor of $\epsilon^{1/2}$ to recover all terms in the governing equation. Hence, an appropriate choice of rescaled dimensionless variables is

$$x = L\xi, \quad z = \epsilon^{1/2} L \zeta, \quad p = p_a - \rho_a g z + \epsilon^{1/2} \Delta \rho g L \, P(\xi, \zeta), \tag{2.11}$$

where ξ, ζ and P are variables that are $\mathcal{O}(1)$ in magnitude. Note that the pressure in (2.11) must also be rescaled by a factor $\epsilon^{1/2}$ so that the boundary condition (2.6) (i.e. $\partial p / \partial z + \rho g = 0$ at $z = 0$)

balances all terms at leading order. In this way, within the boundary layer region, the governing equations and boundary conditions (2.3), (2.5) and (2.6) become

$$\frac{\partial^2 P}{\partial \xi^2} + \frac{\partial^2 P}{\partial \zeta^2} = 0, \tag{2.12}$$

$$\frac{\partial P}{\partial \xi} = 0: \quad \xi = 0 \tag{2.13}$$

and

$$\frac{\partial P}{\partial \zeta} = -1: \quad \zeta = 0. \tag{2.14}$$

In addition, we require that the *inner* solution (within the boundary layer) matches with the *outer* solution (far outside the boundary layer) [26], such that

$$P \to 0: \quad \zeta \to \infty. \tag{2.15}$$

The system is not yet complete since the governing equation (2.12) is a second-order elliptic PDE that requires four boundary conditions. The fourth and final boundary condition needs more careful thought. Since there is a vertical velocity (2.9) descending through the outer region, this induces an arrival of flux $\epsilon u_b L$ within the inner region. However, since this flux can go neither downwards nor leftwards (due to impermeable/symmetric boundaries), it must instead exit through the right-hand boundary, $x = L$. In other words, the right-hand interface must move outwards to conserve mass, creating a new finger-like region of vertical size $z \sim \mathcal{O}(\epsilon^{1/2})$, which we denote region II.[2] Hence, the final boundary condition for region I is given by an integral constraint[3] of the form

$$\int_0^\infty -\left.\frac{\partial P}{\partial \xi}\right|_{\xi=1} \mathrm{d}\zeta = 1. \tag{2.16}$$

The descent of the upper interface in region I and the resulting finger-like region II are both illustrated in figure 1*b*.

Before addressing these details further, we first note that (2.12)–(2.16) can be solved exactly by separation of variables. Hence, the composite solution (valid across both inner and outer regions) is given by

$$p = p_a - \rho_a g z + 2\epsilon^{1/2} \Delta\rho g L \sum_{n=0}^{\infty} \frac{(-1)^n}{\lambda_n^2} \cos\left[\frac{\lambda_n x}{L}\right] \exp\left[-\frac{\lambda_n z}{\epsilon^{1/2} L}\right], \tag{2.17}$$

where $\lambda_n = (2n+1)\pi/2$. Conservation of mass within region I indicates that

$$\phi \frac{\partial h}{\partial t} + \frac{k_H}{\mu} \frac{\partial}{\partial x}\left[\int_0^{h(x,t)} -\frac{\partial p}{\partial x}\, \mathrm{d}z\right] = 0. \tag{2.18}$$

Hence, inserting (2.17) into (2.18) results in the governing equation for the evolution of the thickness of the current, which is

$$\phi \frac{\partial h}{\partial t} - u_b \epsilon L \frac{\partial}{\partial x} \sum_{n=0}^{\infty} \frac{2(-1)^{n+1} \sin \lambda_n x/L}{\lambda_n^2} \left(1 - \exp\left[-\frac{\lambda_n h(x,t)}{\epsilon^{1/2} L}\right]\right) = 0. \tag{2.19}$$

This can be further simplified by ignoring exponentially small terms when h/L is larger than $\mathcal{O}(\epsilon^{1/2})$, and by using the fact that the infinite sum converges to $-x/L$. Hence, we see that the thickness within region I is given by

$$h = H - \frac{\epsilon u_b t}{\phi}, \tag{2.20}$$

which is valid for $0 < x < L$ and for $h \gg \mathcal{O}(\epsilon^{1/2})$. Hence, we see that within this asymptotic framework the shape in region I is independent of x at leading order, $h \approx h(t)$. However, the

[2]By prescribing the growth of a finger-like region II, we have neglected other possible distortions to the right-hand boundary of region I. However, our choice is motivated by comparison with numerical simulations (e.g. figure 2), which clearly show a finger-like region of this form.

[3]The upper limit of the integral in (2.16) is set to ∞ following the method of matched asymptotics [26]. This ensures that mass is exactly conserved as we leave the inner boundary layer solution.

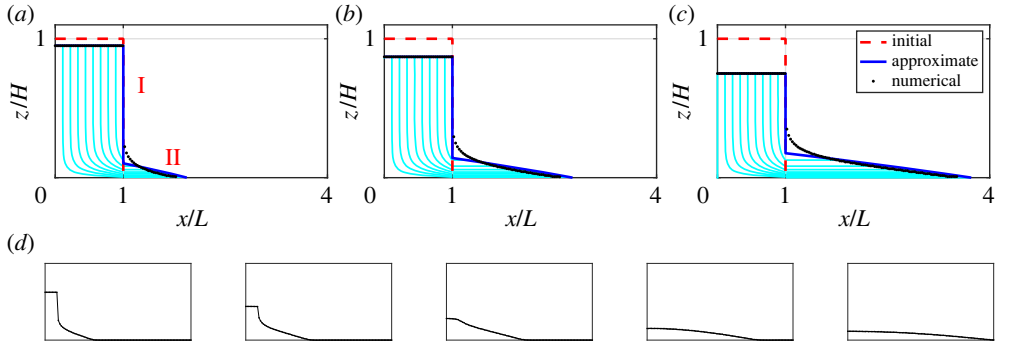

Figure 2. (*a–c*) Approximate solution for regions I and II compared with numerical solution in the case of $\epsilon = 10^{-2}$. Times are given in terms of the transition time (2.37), where (*a*) $t/t^* = 0.07$, (*b*) 0.17 and (*c*) 0.34. Streamlines are evaluated using velocities derived from (2.17) and (2.21). (*d*) Further numerical solutions are shown at times $t/t^* = 0.42, 0.69, 1, 1.82, 3.22$. Note that the aspect ratio of these plots has been stretched for illustration purposes.

dependence of h on x may be recovered by considering higher-order asymptotics (e.g. retaining all terms in (2.19)), or by considering non-rectangular initial shapes (see appendix A).

Next, we address the fluid flow in region II, which is the finger-like region of escaped fluid near the base of the current, which is defined for $L < x < x_n(t)$, where $x_n(t)$ is the maximum extent of the finger. This flow region is long and thin (like a classical gravity current) such that the horizontal velocity is much larger than the vertical velocity. Consequently, the pressure within region II is hydrostatic to good approximation, such that

$$p = p_a - \rho_a g h - \rho g(z - h). \tag{2.21}$$

Similarly to (2.18), conservation of mass within this region gives

$$\phi \frac{\partial h}{\partial t} = u_b \frac{\partial}{\partial x}\left[h \frac{\partial h}{\partial x}\right], \tag{2.22}$$

which is sometimes called the Dupuit approximation. This is accompanied by boundary conditions that correspond with imposing the input flux from region I,

$$-u_b h \frac{\partial h}{\partial x} = \epsilon u_b L: \quad x = L^+, \tag{2.23}$$

and imposing zero thickness and zero flux at the moving front,

$$h \to 0: \quad x \to x_n(t) \tag{2.24}$$

and

$$-u_b h \frac{\partial h}{\partial x} \to 0: \quad x \to x_n(t). \tag{2.25}$$

By introducing dimensionless coordinates,

$$h = \epsilon^{1/2} L\, \mathcal{H}(\xi, \tau), \quad x = L(1 + \xi), \quad t = \frac{\phi L}{\epsilon^{1/2} u_b}\tau, \tag{2.26}$$

we get the same system as [5] for a constant input flux (see appendix B for further details). The solution is well known and is given in terms of the similarity variables

$$\eta = \xi/\tau^{2/3}, \quad \mathcal{H} = \tau^{1/3} f(\eta). \tag{2.27}$$

The self-similar shape function $f(\eta)$ is defined for $\eta \in [0, \eta_N = 1.482]$, and is monotone decreasing from $f_0 := f(0) = 1.296$ to $f(\eta_N) = 0$. The solution for regions I and II is plotted in figure 2*a–c*, at several different times. Streamlines confirm that the flux into region II is fed by the shrinking of region I. Comparison is also made with a numerical solution described later in §3.

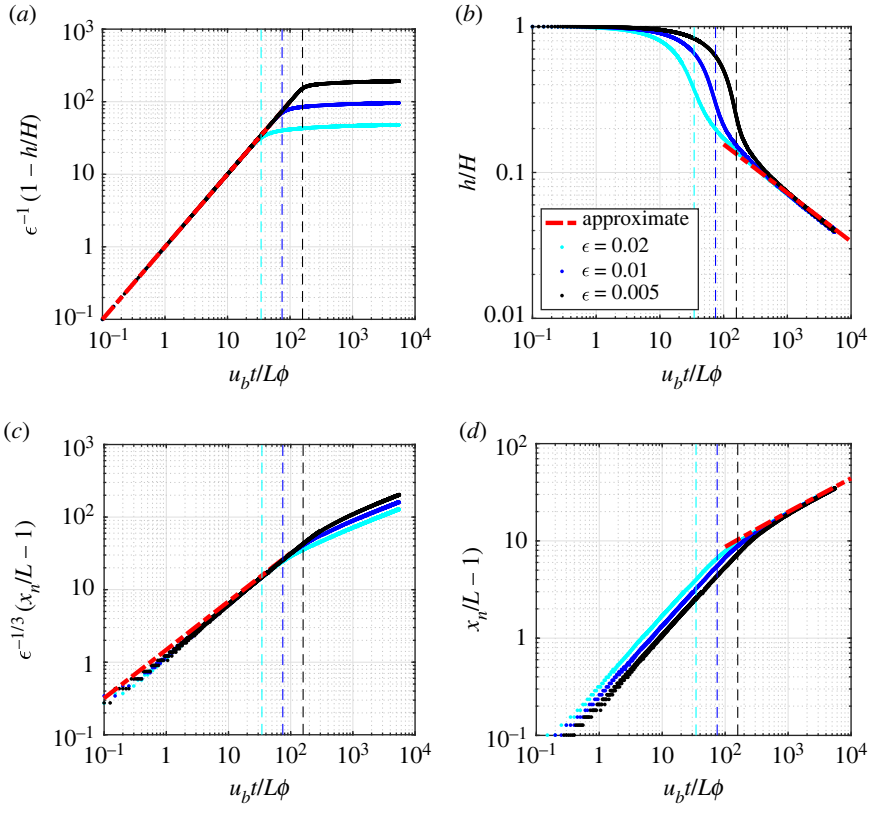

Figure 3. Evolution of the vertical (*a*,*b*) and horizontal (*c*,*d*) extents of the gravity current for different anisotropy values, showing both numerical and approximate solutions. In (*a*,*c*), the results have been rescaled with respect to early-time behaviour, (2.20), (2.28). In (*b*,*d*), the results have been rescaled with respect to late time behaviour, (2.34), (2.35). Vertical dashed lines indicate the transition time t^*. Note that h is taken as its maximum value (which occurs at $x = 0$).

The maximum vertical extent of the flow is given by (2.20), whereas the maximum horizontal extent is determined through the above scalings as

$$x_n = L(1 + \eta_N \tau^{2/3}). \tag{2.28}$$

These are plotted in figure 3*a*,*c*, with dot-dashed red lines, thereby indicating the early-time behaviour of the released fluid.

(b) Transition to self-similarity

After a long time, the flow is expected to eventually transition to the self-similar behaviour of a finite release gravity current [5,12]. As discussed in [18], the late-time dynamics of a two-dimensional gravity current are independent of the anisotropy of the medium since the bulk flow decouples from the ambient.[4] Hence, the anisotropy only affects the late-time behaviour by delaying the time to transition to self-similarity. Hence, to study the late-time behaviour, we first analyse the isotropic case, which determines the late-time dynamics, and then derive the time t^* to transition between the early and late solutions, where t^* depends on the anisotropy ϵ.

As before, the thickness of the gravity current (which now occupies a single region $0 \le x \le x_n(t)$) satisfies the Dupuit approximation (2.22). The boundary conditions are similar to the case

[4]Note that this decoupling is a consequence of ignoring the return flow of ambient fluid, which is in turn ignored because the ambient is presumed to be infinitely deep [23].

of constant input flux, as described above, except the left-hand boundary condition is replaced with the zero flux condition

$$\frac{\partial h}{\partial x} = 0: \quad x = 0. \tag{2.29}$$

Consequently, mass conservation indicates that

$$\int_0^{x_n(t)} h \, \mathrm{d}x = HL. \tag{2.30}$$

By introducing dimensionless coordinates,

$$x = (HL)^{1/2}\xi, \quad h = (HL)^{1/2}\mathcal{H}(\xi, \tau), \quad t = \frac{\phi (HL)^{1/2}}{u_b}\tau, \tag{2.31}$$

and switching to similarity variables

$$\eta = \xi/\tau^{1/3}, \quad \mathcal{H} = f(\eta)/\tau^{1/3}, \tag{2.32}$$

we arrive at a system of equations that can be solved analytically to give

$$f(\eta) = \frac{1}{6}(\eta_N^2 - \eta^2), \tag{2.33}$$

where $\eta_N = 3^{2/3}$, as shown in [5] (see appendix B for further details).

The maximum vertical and horizontal extent of the flow are given by

$$h|_{x=0} = \frac{\eta_N^2 (HL)^{1/2}}{6\tau^{1/3}} \tag{2.34}$$

and

$$x_n = \eta_N (HL)^{1/2} \tau^{1/3}, \tag{2.35}$$

respectively. These scalings are plotted in figure 3*b*,*d*, with dot-dashed red lines, thereby indicating the late-time behaviour of the gravity current.

Next, we discuss the time taken to transition from the early flow regime involving two fluid regions to the late flow regime with a single region which is self-similar. In the early regime, the vertical extent of region I descends according to (2.20). By contrast, the vertical extent of region II ($\epsilon^{1/2} L\mathcal{H}$ in (2.26)) increases like $\sim f_0 (u_b \epsilon^2 L^2 t/\phi)^{1/3}$. Hence, it is expected that the transition to self-similarity will occur once these two thickness scalings approach each other. Thus, the transition time t^* satisfies the cubic equation

$$\left(H - \frac{\epsilon u_b t^*}{\phi}\right)^3 = \frac{f_0^3 u_b \epsilon^2 L^2 t^*}{\phi}. \tag{2.36}$$

The solution has a complicated form but can be expanded in powers of $\epsilon \ll 1$ to give

$$t^* = \frac{L\phi}{u_b \epsilon}\left[\alpha - f_0 \alpha^{1/3} \epsilon^{1/3} + \frac{f_0^2}{3\alpha^{1/3}}\epsilon^{2/3} + \cdots\right], \tag{2.37}$$

where $\alpha = H/L$ is the aspect ratio of the initial current shape. Hence, anisotropy delays the transition to a classical self-similar regime, which is consistent with other studies [18]. At the transition time t^*, the maximum thickness of the current (which we denote H^*) is given by

$$H^* = L\epsilon^{1/3}\left[f_0 \alpha^{1/3} - \frac{f_0^2}{3\alpha^{1/3}}\epsilon^{1/3} + \ldots\right]. \tag{2.38}$$

This indicates that, by the time transition occurs for very anisotropic media, the bulk of the current has shrunk significantly. This hints towards a reduced swept volume, which we analyse further in §4.

The transition time t^* and the transition thickness H^* (given in dimensionless terms) are plotted in figure 4. These importantly depend on both the anisotropy ϵ as well as the initial aspect ratio of the flow α. It should be noted that in practice strong anisotropy $\epsilon \ll 1$ may cause the flow

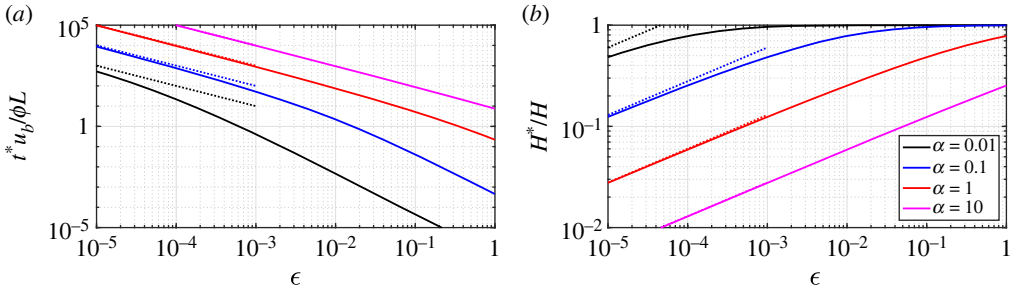

Figure 4. (*a*,*b*) Transition time t^* and the transition thickness H^*, determined by solving (2.36) for different values of the anisotropy ϵ and the initial aspect ratio α. Leading order scalings for small ϵ (see (2.37), (2.38)) are shown with dotted lines.

to spread out laterally before contact with the impermeable cap rock [17]. Therefore, $\epsilon \ll 1$ may be correlated with $\alpha \ll 1$, although this also depends on the location of the injection (see §6).

3. Finite difference computations of Darcy flow

Next, in this section, we compare our analytical predictions with finite difference computations of two-dimensional Darcy flow. The flow is modelled with the Darcy equations (2.1)–(2.2), accounting for different permeability values, k_H and k_V, in the horizontal and vertical directions. The governing equations are accompanied by boundary conditions (2.5)–(2.6), corresponding with impermeable/symmetric walls at $x = 0$ and $z = 0$. The dynamic boundary condition (2.7) is imposed on the interface $z = h(x, t)$, which is interpolated over a gridded mesh of 150 × 150 points. Likewise, a spatial domain of finite size $4L \times H$ is chosen in the $x \times z$ directions. The fluid flow is not resolved beyond the interface $z > h(x, t)$ since pressure is assumed to be hydrostatic in the ambient fluid.[5] Mass conservation dictates that the interface evolves according to

$$\phi \frac{\partial h}{\partial t} + \frac{k_H}{\mu} \frac{\partial}{\partial x} \left[\int_0^{h(x,t)} - \frac{\partial p}{\partial x} \, \mathrm{d}z \right] = 0, \tag{3.1}$$

with suitable initial conditions $h(x, 0) = h_0(x)$. Boundary conditions for h are given by (2.24), (2.25) and (2.29) (see earlier discussion for further explanation). The time-dependent equation for the fluid–fluid interface (3.1) is solved using an explicit forward Euler scheme in time, and a backward scheme in space. At each time step the Darcy equations, (2.1)–(2.2), are solved using a second-order central finite difference scheme. The code used for these computations is available in the electronic supplementary material.

Results from the finite difference computations are compared with the analytical model in figures 2 and 3. Figure 2*a–c* shows the distorted spreading of the gravity current via a thin finger near the base. Good agreement is observed everywhere except near $x \approx L$ where the two regions connect. Here, the interface transitions smoothly between regions I and II, which is a second-order feature that is missing from the simple analytical model. The numerical solution enables computation of the gravity current shape up to and beyond the transition time t^*, as is displayed in figure 2*d*. This demonstrates clearly how the flow transitions from a two-region (bulk/finger) structure at early times to a slumping single-region structure at late times.

Figure 3 displays numerical computations of the vertical and horizontal extents of the gravity current across early and late time regimes. Different values of ϵ are evaluated, and the results are rescaled to collapse the data at early and late times separately. The data show good agreement with the analytical predictions, with error getting smaller as we decrease ϵ, as expected. Likewise,

[5]In reality, the ambient fluid is not perfectly quiescent, since it gets displaced by the gravity current, but such displacement flow does not affect the gravity current to good approximation since the ambient fluid is of infinite depth [23].

we also observe good agreement with the transition times (shown with vertical dashed lines), indicating the accuracy of our prediction for t^* (2.37).

As a benchmark test, we also compare these finite difference computations with a gravity current slumping in an isotropic medium, $\epsilon = 1$. Since our analytical model only applies for $\epsilon \ll 1$, the initial dynamics involving regions I and II are irrelevant for this case. Instead, we set the initial shape as

$$h_0(x) = H\left[1 - \left(\frac{x}{L}\right)^2\right], \tag{3.2}$$

which is simply the similarity solution (2.33). Since the initial shape satisfies the similarity conditions, this ensures that the solution remains self-similar for all time. In figure 8*a–c*, we plot the self-similar evolution of the gravity current shape at various times. Excellent agreement is attained between the numerical model and the exact self-similar solution, indicating the reliability of the finite difference approach. In figure 8*d–f*, we display similar computations for the same initial shape released in an anisotropic medium, $\epsilon = 10^{-2}$. In this case, the flow is decomposed into regions I and II, as before, demonstrating how our simple model can be extended to account for other released shapes. Further details and discussion of this case are given in appendix A.

4. Swept shape and swept volume

As described earlier, it is useful for applications (e.g. contaminant transport or CO_2 storage) to quantify the total volume contacted by the gravity current, also known as the swept volume.[6] At early times $t \ll t^*$, region I shrinks uniformly downwards while region II grows upwards and outwards. Hence, the swept volume $\mathcal{V}$ is simply equal to the initial volume plus the instantaneous volume of region II, such that

$$\mathcal{V}(t) = 2HL + 2\epsilon u_b L t. \tag{4.1}$$

At much later times $t \gg t^*$, once the gravity current has transitioned to self-similarity, the thickness $z = h(x,t)$ has some parts which are growing and other parts which are shrinking, so this requires more careful attention. To deal with this, we first define the swept shape $\mathcal{S}$ as the maximum thickness that the current ever reached at a given value of x, such that

$$\mathcal{S}(x) = \max_t\{h(x,t)\}. \tag{4.2}$$

The swept volume is then given in terms of $\mathcal{S}$ as

$$\mathcal{V}(t) = 2\int_0^{x_n(t)} \mathcal{S}\,\mathrm{d}x. \tag{4.3}$$

The swept shape (4.2) is calculated by finding the time at which the thickness is maximal, which is equivalent to $\eta = 3^{1/6}$ in the similarity solution f (2.33). Inserting this into (4.2), we get

$$\mathcal{S}(x) = \frac{HL}{3^{1/2}x}, \tag{4.4}$$

which is only valid for $x \gg L$. Hence, the swept volume (up to a constant C) is

$$\mathcal{V}(t) = \frac{2HL}{3^{1/2}}\log x_n(t) + C, \tag{4.5}$$

which clearly diverges like $\sim \log t$ as $t \to \infty$. The constant of integration is found by equating (4.1) and (4.5) at the transition time t^*. Hence, the late time behaviour of the swept volume is given by

$$\mathcal{V}(t) = 2HL + 2\epsilon u_b L t^* + \frac{2HL}{3^{1/2}}\log\left(\frac{t}{t^*}\right)^{1/3}. \tag{4.6}$$

In figure 5*a*,*b*,*d*, the swept shape $\mathcal{S}(x)$ and swept volume $\mathcal{V}(t)$ are plotted for different values of the anisotropy ϵ. For $\epsilon \ll 1$, the anisotropy restricts the swept shape (for $x > L$) to finger-like regions

[6]Note that since our model is in two dimensions, the swept volume is taken as per unit width. Also note that the total volume of fluid is constant and given by $2HL\phi = \phi\mathcal{V}(0)$.

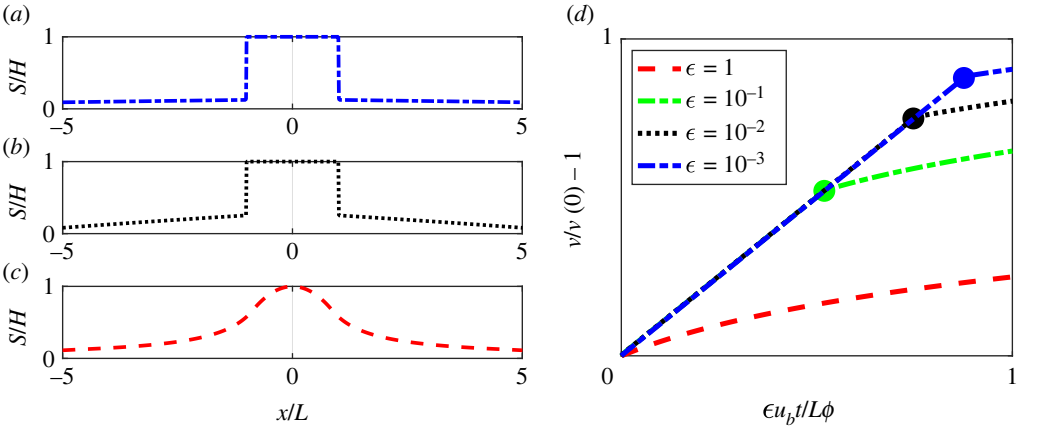

Figure 5. (*a*,*b*) Swept shape of the gravity current $\mathcal{S}(x)$ (4.2) in the case of $\epsilon = 10^{-3}$ and 10^{-2}. (*c*) Self-similar isotropic case $\epsilon = 1$ (note the modified initial conditions). (*d*) Evolution of the swept volume $\mathcal{V}(t)$ for each of these cases (note that time is stretched by a factor ϵ). Transition times t^* are indicated with coloured dots. The initial aspect ratio is set as $\alpha = 1$ in all cases.

near the base of the current. The maximum thickness of the fingers is set by H^* (2.38), which scales like $H^* \sim \epsilon^{1/3}$ (i.e. the more anisotropic the medium, the narrower the fingers). Furthermore, anisotropy delays the transition time (2.37), since $t^* \propto \epsilon^{-1}$. Meanwhile, before transition occurs, $t \ll t^*$, anisotropy causes the swept volume to grow slowly (since $\mathcal{V} \propto \epsilon t$ in (4.1)), such that the gravity current contacts a smaller fraction of pore space at early times. Note that the kinks at the corners $x = \pm L$ (in $\mathcal{S}$) and at the transition time $t = t^*$ (in $\mathcal{V}$) would be smoothed out by higher-order asymptotics or numerical computations of two-dimensional Darcy flow. However, such features do not affect the overall leading order behaviour displayed here.

For comparison, we also plot the swept shape $\mathcal{S}$ in the isotropic case, $\epsilon = 1$, in figure 5*c*. As described at the end of §3, the isotropic case uses (3.2) as the initial shape and remains self-similar for all times. It should be noted that the modified initial shape results in a different initial swept volume for this case, $\mathcal{V}(0) = 4HL/3$. Clearly, the classical (isotropic) self-similar solution has a larger swept shape and a faster growing swept volume than the anisotropic cases.

5. Finite release with radial symmetry

The above results can be easily extended to account for radially symmetric flows if the anisotropy remains aligned with the vertical coordinate, i.e. with permeability k_H, k_V in the radial/vertical directions. To extend the model from the two-dimensional case, we take the impermeable boundary to be the horizontal plane, $z = 0$. Likewise, we consider the released shape to be a cylinder of initial height H and radius R. Since the initial shape of the current is radially symmetric, it will spread out and remain radially symmetric for all times.

Following the derivation in §2a, the thickness of the current evolves according to (2.20) at early times. This results in a radial flux of magnitude $\epsilon u_b \pi R^2$ exiting region I ($0 \le r \le R$) into a growing annular region II ($R \le r \le r_n(t)$) at the base of the current. Conservation of mass within region II gives

$$\phi \frac{\partial h}{\partial t} = u_b \frac{1}{r} \frac{\partial}{\partial r} \left[rh \frac{\partial h}{\partial r} \right]. \tag{5.1}$$

Boundary conditions correspond with imposing the input flux from region I,

$$-2\pi u_b r h \frac{\partial h}{\partial r} = \epsilon u_b \pi R^2 : \quad r = R^+, \tag{5.2}$$

and imposing zero thickness and zero flux at the moving front,

$$h \to 0: \quad r \to r_n(t) \tag{5.3}$$

and

$$-2\pi r u_b h \frac{\partial h}{\partial r} \to 0: \quad r \to r_n(t). \tag{5.4}$$

By introducing dimensionless coordinates,

$$h = (\pi\epsilon)^{1/2} R\,\mathcal{H}(\xi,\tau), \quad r = R(1+\xi), \quad t = \frac{\phi R}{(\pi\epsilon)^{1/2} u_b}\tau, \tag{5.5}$$

we get a similar system to [27] (see appendix B for further details). The solution is given in terms of the similarity variables

$$\eta = \xi/\tau^{1/2} \quad \text{and} \quad \mathcal{H} = f(\eta). \tag{5.6}$$

The shape function $f(\eta)$ is defined for $0 < \eta \le \eta_N = 1.155$, but has an unphysical singularity at the origin. This singularity, which is due to a breakdown of the hydrostatic assumption, can be addressed by introducing a non-hydrostatic (i.e. source-driven) region near the origin, as discussed in [18]. However, for the sake of simplicity, we ignore such details for the present study. For our purposes, (5.6) serves as a good approximation for the finger-like growth of region II (i.e. for $r \gg R$). The transition time t^* is found by matching the two thicknesses of regions I and II, such that

$$H - \frac{\epsilon u_b t^*}{\phi} = (\pi\epsilon)^{1/2} R. \tag{5.7}$$

Hence, the transition time and thickness are given by

$$t^* = \frac{\phi R}{\epsilon u_b}(\alpha - (\pi\epsilon)^{1/2}) \tag{5.8}$$

and

$$H^* = (\pi\epsilon)^{1/2} R, \tag{5.9}$$

where in this case the initial aspect ratio is $\alpha = H/R$. Much later than the transition time $t \gg t^*$, the flow continues to slump as a single region, similar to §2b. In this case, the entire thickness satisfies (5.1). The boundary condition (5.2) is replaced by a zero flux condition at the origin, which is

$$\frac{\partial h}{\partial r} = 0: \quad r = 0. \tag{5.10}$$

Hence, mass conservation indicates that

$$2\pi \int_0^{r_n(t)} rh\,\mathrm{d}r = \pi H R^2. \tag{5.11}$$

By introducing dimensionless coordinates,

$$r = (HR^2)^{1/3}\xi, \quad h = (HR^2)^{1/3}\mathcal{H}(\xi,\tau), \quad t = \frac{\phi (HR^2)^{1/3}}{u_b}\tau, \tag{5.12}$$

and switching to similarity variables

$$\eta = \xi/\tau^{1/4} \quad \text{and} \quad \mathcal{H} = f(\eta)/\tau^{1/2}, \tag{5.13}$$

we arrive at a system of equations that can be solved analytically to give

$$f(\eta) = \frac{1}{8}(\eta_N^2 - \eta^2), \tag{5.14}$$

where $\eta_N = 2$ (see appendix B for further details).

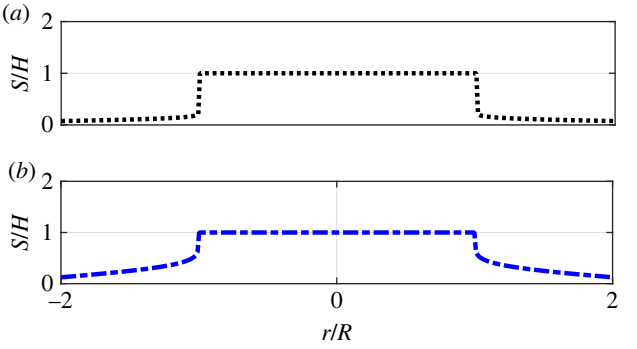

Figure 6. Swept shape of the gravity current $\mathcal{S}(r)$ in the radially symmetric case. Initial aspect ratio is set to $\alpha = 0.2$ and the anisotropy is set to (*a*) $\epsilon = 10^{-3}$ and (*b*) $\epsilon = 10^{-2}$.

Next, let us briefly discuss the swept shape and swept volume for this case. At early times $t \ll t^*$, the swept volume $\mathcal{V}$ is equal to the initial volume plus the instantaneous volume of region II, such that

$$\mathcal{V}(t) = \pi HR^2 + \epsilon u_b \pi R^2 t. \tag{5.15}$$

At much later times $t \gg t^*$, the swept shape $\mathcal{S}(r)$ is calculated by finding the time at which the current thickness is maximal, which is equivalent to $\eta = 2^{1/2}$ in the similarity solution f (5.14). Hence, the swept shape is

$$\mathcal{S}(r) = \frac{HR^2}{2r^2}, \tag{5.16}$$

which is only valid for $r \gg R$. The swept volume, which is now defined as

$$\mathcal{V}(t) = 2\pi \int_0^{r_n(t)} r\mathcal{S}\, \mathrm{d}r, \tag{5.17}$$

is calculated (following similar steps as in §4) for late times as

$$\mathcal{V}(t) = \pi HR^2 + \epsilon u_b \pi R^2 t^* + \pi HR^2 \log\left(\frac{t}{t^*}\right)^{1/4}. \tag{5.18}$$

To illustrate the radially symmetric case, the swept shape $\mathcal{S}(r)$ is plotted in figure 6*a*,*b*, for $\epsilon = 10^{-3}$ and 10^{-2}. As with the two-dimensional case, stronger anisotropy results in a reduced swept shape (i.e. smaller values of $\mathcal{S}$ for $r > R$). Likewise, although not plotted, the swept volume increases slowly like $\mathcal{V} \propto \epsilon t$ before transition to self-similarity, indicating that anisotropy reduces the contacted volume of pore space.

6. Modelling CO_2 storage in an anisotropic reservoir: injection and post-injection regimes

In the following section, we apply the models from the present study to account for a typical injection scenario in a CO_2 storage site. Motivated by the Goldeneye field study of [17] (see fig. 4 of that paper), we consider an aquifer into which CO_2 is injected at a constant rate $Q = 2.3 \times 10^{-6}\,\mathrm{m^2\,s^{-1}}$ (per unit width) at a depth of $D = 40\,\mathrm{m}$ below an impermeable cap rock for a period of 10 years before being switched off. Unlike in the previous sections, here we consider an inverted flow scenario, in which a less dense fluid (CO_2) is released inside a more dense fluid (brine). However, the dynamics derived in earlier sections still apply here according to the Boussinesq approximation [22]. We assume that the reservoir has porosity

$\phi = 0.23$ and anisotropy $\epsilon = 0.005$–0.01. Furthermore, we take the buoyancy velocity[7] of the CO_2 to be $u_b = 1.65 \times 10^{-5}$ m s^{-1}. Initially, it takes a time $t = D\phi/\epsilon u_b = 1.8$ years for the injected CO_2 to reach the cap rock, after which the flow begins spreading laterally, as described by our model.

First, let us describe the regime of constant injection. Once injected, the CO_2 rises upwards as a buoyant plume until it reaches the impermeable cap rock. It is well known that buoyant plumes expand as they rise due to both miscible and multi-phase phenomena. The study of [28] shows that dispersive mixing between the injected and ambient phase causes the total plume width to grow like $\sim\sqrt{\phi\alpha z}$, where α is the transverse dispersivity. Hence, we might expect that during the 40 m distance over which the plume rises vertically, it may widen by a factor $\sqrt{40} \approx 6.3$. In practice, it is likely to widen much more than this because of heterogeneity and/or anisotropy (i.e. via obstruction due to horizontal sedimentary layers). Furthermore, as shown in [17,29,30], small-scale capillary forces (associated with heterogeneity) can significantly enhance the lateral spreading of the plume. In the present study, we neglect such effects for the sake of simplicity, and instead model the plume as a straight column with a constant density difference $\Delta\rho$ between the injected and ambient phase. In this way, the whole plume rises at speed $w = \epsilon u_b$ and the plume width is given by $d = Q/\epsilon u_b \approx 14$ m.

The results in this section are obtained by connecting the two-dimensional analytical model from §2*a*,*b* with a simple model for the plume as a rectangular region of buoyant fluid rising at speed $w = \epsilon u_b$. The only difference between the models used here and in the previous sections is the inclusion of this vertically rising plume (as well as the field-specific parameter values used). Initially we model the plume as a rectangular column that begins rising vertically from the injection point until it encounters the impermeable cap rock, which happens after 1.8 years. After this, the plume feeds the lateral spread of finger-like regions at the base of the cap rock, just as described before (except without the shrinking of region I, since the plume is continuously replenished by the injection point). Once injection stops after 10 years, the remaining plume (now region I) begins to shrink as it migrates towards the cap rock. Eventually, once the thicknesses of regions I and II become equal, the flow transitions to a self-similar gravity current, slumping beneath the cap rock as described earlier.

In figure 7*a*–*c*, we illustrate the development of the flow at 5, 11 and 20 years after injection begins, in the case where $\epsilon = 0.01$. At 5 years, we can already observe significant growth of the thin fingers of CO_2 (which first commenced after 1.8 years). After 10 years injection stops, and after 11.8 years, the remaining fluid in the plume column has risen upwards and reached the cap rock. After this, the flow transitions to a single gravity-driven region which spreads out in a self-similar fashion, as can be seen by the profile much later at 20 years. We have also compared these analytical predictions with finite difference computations (see §3) applied to the same scenario. Much like the plots in figure 2*a*–*c*, we find close comparison between the numerical and analytical results, so we do not include them again here.

In figure 7*d*–*f*, similar plots are shown for an aquifer with $\epsilon = 0.005$. In order to use the same plume width as above, the input flux must be halved since $Q = \epsilon u_b d$ is proportional to the anisotropy. To correct this, we have also included plots in figure 7*g*–*i*, of the same scenario but with double the plume width (i.e. approx. 28 m) to maintain the same input flux. The justification for a wider plume is that stronger anisotropy tends to enhance the lateral spreading of the CO_2 [17]. However, by halving the value of ϵ, it takes twice as long for the plume to initially reach the cap rock compared with figure 7*a*–*c* (since the rise speed is $w = \epsilon u_b$). Hence, the finger-like regions only emerge after 3.6 years instead of 1.8 years.

Although we have considered an example here in which the CO_2 is injected far below the cap rock, other scenarios may have an injection point much closer to $z = 0$. In such cases, the dynamics during injection are described in [18], in which it was shown that the flow is either in a pressure-driven or a gravity-driven regime, depending on the time scale of injection and the anisotropy.

[7]The buoyancy velocity (2.10) is calculated using parameter values listed in [17], which are $k = \exp(52.544\phi - 6.4656)$ mD, $\mu = 5.66 \times 10^{-5}$ Pa.s and $\Delta\rho = 1023.34$–691.22 kg m^{-3}.

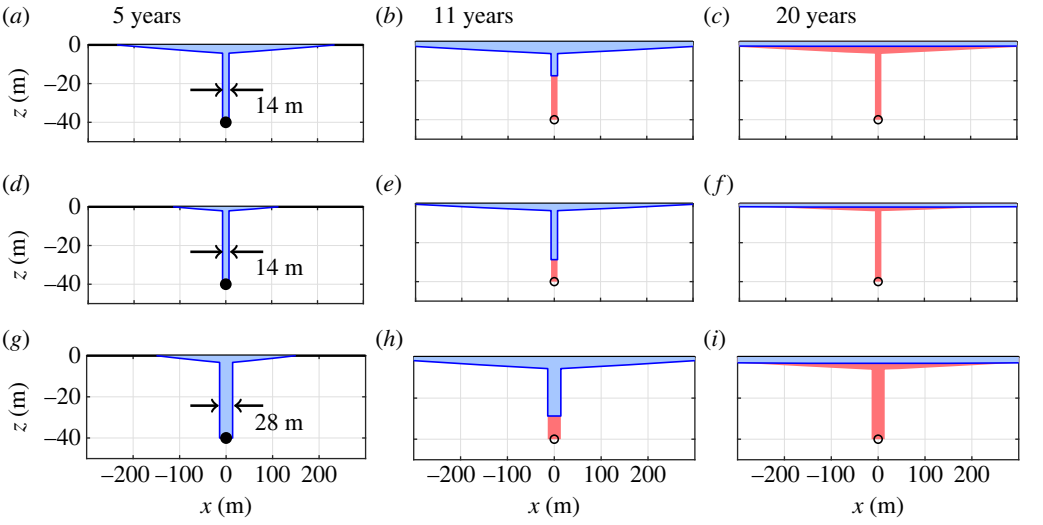

Figure 7. Case study in which CO_2 is injected into an anisotropic reservoir 40 m below an impermeable cap rock for a period of 10 years before injection is switched off. (*a–c*) $\epsilon = 0.01$ and $Q = 2.3 \times 10^{-6}$ m^2 s^{-1}. (*d–f*) $\epsilon = 0.005$ and $Q = 1.15 \times 10^{-6}$ m^2 s^{-1}. (*g–i*) $\epsilon = 0.005$ and $Q = 2.3 \times 10^{-6}$ m^2 s^{-1}, incorporating a wider plume. In each case, the swept shape of the plume is shown with red shading. Black circles represent the injection point and are shaded to indicate an injection regime or hollow to indicate a post-injection regime.

Once injection is switched off the remaining fixed volume of fluid continues spreading according to the dynamics discussed in the present study. As such, there is an initial period of time in which the flow is restricted to a boundary layer near the cap rock, after which the flow transitions to classical self-similar spreading [12]. However, we do not go into the details of this case since the key ideas have already been discussed.

7. Discussion

The gravity-driven spreading of a finite volume of fluid in anisotropic porous media differs from the isotropic case since the vertical flow is restricted by the permeability $k_V \ll k_H$. In the initial dynamics, the bulk of the flow descends slowly with a boundary layer near the impermeable base that diverts the flow into thin finger-like regions growing slowly in the lateral direction. This partition of the flow into bulk and finger regions reduces the swept volume of the gravity current compared with the isotropic case. This indicates that released volumes in anisotropic aquifers contact a smaller fraction of the available pore space. Hence, the spread of a contaminant in an anisotropic aquifer may be easier to contain since the contacted volume is reduced. By contrast, in the case of CO_2 sequestration, where the aim is to trap as much CO_2 in the pore space as possible, isotropic aquifers may have better potential in terms of residual trapping (which is a function of the contacted volume of pore space), though this ignores other trapping mechanisms such as dissolution, structural trapping and mineralization [19].

It is important to consider the possible limitations of this model for such realistic scenarios. First and foremost, it must be noted that the anisotropic permeability values k_H, k_V, are upscaled quantities that attempt to capture the macroscopic effect of small-scale heterogeneities on the flow. These upscaled quantities are only a good approximation when the vertical length scale of the flow H is much larger than the heterogeneity length scale (e.g. the width of sedimentary layers) or when the permeable interval is inherently anisotropic due to compaction effects. If this is not the case, more complex flow models are required to treat the spread of fluid beneath and through successive layers [3,31,32].

Another consideration for the case of CO_2 sequestration is the effect of trapped saturation on the dynamics and spreading of the current. As the current moves, a fraction of its mass is lost to residual trapping due to small-scale capillary forces [19] and dissolution within the surrounding brine [8]. According to some trapping models [7], this can arrest the spread of the current altogether. Likewise, the spreading could also be arrested by lateral heterogeneities in the capillary pressure pinning the nose of the gravity current.

While the conclusion of this study is that anisotropy reduces the swept volume of the gravity current, this does not take into account the enhanced trapping potential due to changes in the capillary pressure across heterogeneities, also known as capillary heterogeneity trapping [33]. Specifically, during the imbibition cycle small-scale capillary forces induce a build-up of saturation beneath each sedimentary layer that can account for as much as 14% of the overall trapped saturation. Hence, the optimum anisotropy will no doubt strike a balance between the trapping associated with these heterogeneities and the reduction in swept volume that they induce.

It is also worth mentioning the flow of the ambient fluid, which we have so far ignored for this study. In particular, the flow of the ambient fluid may affect the gravity current dynamics whenever there are restrictions to the local ambient displacement, such as may result from confinement due to sedimentary strata. In such cases, the viscosity contrast between the released and ambient fluids can modify the shape of the current [23] and cause fingering instabilities [34]. In the context of carbon sequestration, CO_2 is typically 20–30 times less viscous than brine. As shown in [23] for confined porous layers, this viscosity contrast causes an enhanced spreading of the CO_2 in the shape of a thin finger along the cap rock. Hence, this viscosity contrast distorts the spreading of CO_2 in a similar manner to anisotropy, as studied here. Therefore, the expected effect of a viscosity contrast in confined anisotropic media is an extremely pronounced finger-like intrusion of CO_2.

In relation to the above discussion, it is interesting to consider the possible scenarios in which an 'exchange' flow (i.e. when horizontal velocities become negative within the gravity current) may occur [35]. As shown by the streamlines in figure 2 (and confirmed by numerical simulations), the flows we have so far studied exclusively have fluid draining from region I into region II. Under certain conditions, however, a return flow may be observed, which is of practical significance since it would enhance mixing with the ambient. This could be considered either advantageous in the case of CO_2 sequestration or disadvantageous in the case of a contaminant spill. Such exchange flows may occur for initial shapes that are sufficiently non-convex (i.e. so that as they slump some areas of flow are reversed), or if the ambient fluid is confined. These scenarios, which we leave for a future study, would require careful modelling of both released and ambient phases, and could include an anisotropic permeability field and/or a set of bounding sedimentary strata.

Data accessibility. The finite difference code used in this study can be found in the electronic supplementary material or on the personal website of the author: https://maths.ucd.ie/~gbenham/openaccess.zip.

Supplementary material is available online [36].

Declaration of AI use. I have not used AI-assisted technologies in creating this article.

Author's contributions. G.P.B.: conceptualization, formal analysis, investigation, methodology, project administration, resources, validation, visualization, writing—original draft, writing—review and editing.

Conflict of interest declaration. I declare I have no competing interests.

Funding. No funding has been received for this article.

Acknowledgements. The author wishes to thank the anonymous peer reviewers for time taken to review the manuscript.

Appendix A. Additional plots

In this section, we present some additional plots comparing the numerical solution from §3 with various approximate and analytical solutions. While in the previous sections, a rectangular shape was chosen for the initial released shape of dense fluid, here we consider a curved profile with

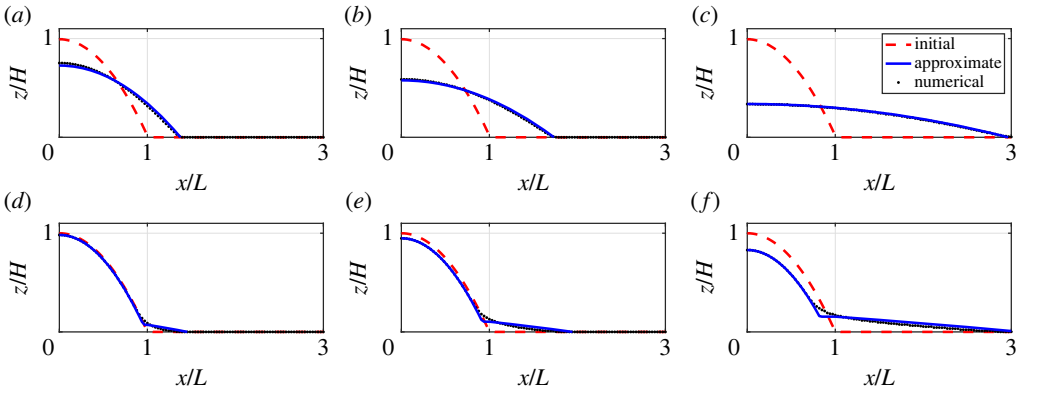

Figure 8. Evolution of a gravity current with initial shape given by (3.2) in the case of an isotropic medium $\epsilon = 1$ (*a–c*) and an anisotropic medium $\epsilon = 10^{-2}$ (*d–f*). Dimensionless times are given by $u_b t/L\phi = 0.87, 1.74, 8.68$ in (*a–c*) and $1.70, 5.09, 17.0$ in (*d–f*).

initial shape $h_0(x)$ given by (3.2). In the case of an isotropic medium $\epsilon = 1$, this results in immediate self-similar behaviour, as described in §2b. We use the analytical self-similar solution (2.33) as a means of verifying our numerical method. In figure 8*a–c*, profiles of the gravity current are shown at three different times. Overall, very good agreement is found, indicating the soundness of the numerical method.

Unfortunately, no benchmark analytical solution exists for anisotropic porous media, but we can nevertheless compare against the approximate solution derived in this study. In figure 8*d–f*, plots are shown for the same curved initial shape (3.2) released in an anisotropic medium with $\epsilon = 10^{-2}$. It is straightforward to extend the approximate solution derived earlier to this initial shape. As such, the bulk fluid region I initially evolves according to

$$h = h_0(x) - \frac{\epsilon u_b t}{\phi}. \tag{A 1}$$

Meanwhile, region II initially evolves according to the self-similar dynamics (2.27), which correspond with a finger-like region fed by a constant input flux $\epsilon u_b L$ from region I (see §2a). These two solutions are then simply joined together to make the plots in figure 8*d–f*. Overall, good agreement is achieved, indicating that our model can be extended to this and other such similar initial shapes.

Appendix B. Further details on similarity solutions

In this section, we summarize the equations that define the different similarity solutions used in the main text. Let us start with the two-dimensional equations for region II at early times. In this case, the system of equations deriving from (2.22)–(2.25) after applying coordinate transformations (2.26)–(2.27) is

$$\frac{1}{3}f - \frac{2}{3}\eta\frac{\mathrm{d}f}{\mathrm{d}\eta} = \frac{\mathrm{d}}{\mathrm{d}\eta}\left[f\frac{\mathrm{d}f}{\mathrm{d}\eta}\right], \tag{B 1}$$

$$-f\frac{\mathrm{d}f}{\mathrm{d}\eta} = 1: \quad \eta = 0, \tag{B 2}$$

$$f = 0: \quad \eta = \eta_N \tag{B 3}$$

and

$$-f\frac{\mathrm{d}f}{\mathrm{d}\eta} = 0: \quad \eta = \eta_N. \tag{B 4}$$

These can be solved numerically for the shape function $f(\eta)$ and prefactor $\eta_N = 1.482$.

Next, we summarize the two-dimensional equations at late times, once the gravity current has transitioned to a single slumping region. In this case, the system of equations (2.22), (2.24), (2.29), (2.30), after applying coordinate transformations (2.31)–(2.32), becomes

$$-\frac{1}{3}f-\frac{1}{3}\eta\frac{\mathrm{d}f}{\mathrm{d}\eta}=\frac{\mathrm{d}}{\mathrm{d}\eta}\left[f\frac{\mathrm{d}f}{\mathrm{d}\eta}\right], \tag{B 5}$$

$$f=0:\quad \eta=\eta_N, \tag{B 6}$$

$$\frac{\mathrm{d}f}{\mathrm{d}\eta}=0:\quad \eta=0 \tag{B 7}$$

and

$$\int_0^{\eta_N} f\,\mathrm{d}\eta=1. \tag{B 8}$$

These can be solved analytically to give (2.33) and $\eta_N=3^{2/3}$.

In the radially symmetric case, the governing equations for region II at early times are (5.1)–(5.4). Hence, after applying the coordinate transformations (5.5)–(5.6), we get the system of equations

$$-\frac{1}{2}\eta\frac{\mathrm{d}f}{\mathrm{d}\eta}=\left(\frac{1}{1+\eta\tau^{1/2}}\right)\frac{\mathrm{d}}{\mathrm{d}\eta}\left[(1+\eta\tau^{1/2})f\frac{\mathrm{d}f}{\mathrm{d}\eta}\right], \tag{B 9}$$

$$-2\pi\left(\frac{1+\eta\tau^{1/2}}{\tau^{1/2}}\right)f\frac{\mathrm{d}f}{\mathrm{d}\eta}=1:\quad \eta=0, \tag{B 10}$$

$$f=0:\quad \eta=\eta_N \tag{B 11}$$

and

$$-2\pi\left(\frac{1+\eta\tau^{1/2}}{\tau^{1/2}}\right)f\frac{\mathrm{d}f}{\mathrm{d}\eta}=0:\quad \eta=\eta_N. \tag{B 12}$$

After sufficiently long times $1\ll\tau\ll\tau^*$ (where τ^* is the dimensionless transition time), the time-dependence is removed from the above system. In other words, we consider when enough time has passed that the finger has grown far from the initial shape, but not so long for transition to occur. In this case, the system of equations simplifies to

$$-\frac{1}{2}\eta\frac{\mathrm{d}f}{\mathrm{d}\eta}=\frac{1}{\eta}\frac{\mathrm{d}}{\mathrm{d}\eta}\left[\eta f\frac{\mathrm{d}f}{\mathrm{d}\eta}\right], \tag{B 13}$$

$$-2\pi\eta f\frac{\mathrm{d}f}{\mathrm{d}\eta}=1:\quad \eta=0, \tag{B 14}$$

$$f=0:\quad \eta=\eta_N \tag{B 15}$$

and

$$-2\pi\eta f\frac{\mathrm{d}f}{\mathrm{d}\eta}=0:\quad \eta=\eta_N. \tag{B 16}$$

These can be solved numerically for the shape function $f(\eta)$ and prefactor $\eta_N=1.155$.

Finally, we summarize the radially symmetric equations at late times, once the gravity current has transitioned to a single slumping region. In this case, the system of equations (5.1), (5.3), (5.10), (5.11), after applying coordinate transformations (5.12)–(5.13), becomes

$$-\frac{1}{2}f-\frac{1}{4}\eta\frac{\mathrm{d}f}{\mathrm{d}\eta}=\frac{1}{\eta}\frac{\mathrm{d}}{\mathrm{d}\eta}\left[\eta f\frac{\mathrm{d}f}{\mathrm{d}\eta}\right], \tag{B 17}$$

$$f=0:\quad \eta=\eta_N, \tag{B 18}$$

$$\frac{\mathrm{d}f}{\mathrm{d}\eta}=0:\quad \eta=0 \tag{B 19}$$

and $$2\int_0^{\eta_N} \eta f \, \mathrm{d}\eta = 1. \tag{B 20}$$

These can be solved analytically to give (5.14) and $\eta_N = 2$.

References

1. Guérin A, Devauchelle O, Lajeunesse E. 2014 Response of a laboratory aquifer to rainfall. *J. Fluid Mech.* **759**, R1. (doi:10.1017/jfm.2014.590)
2. Bear J, Cheng A. 2010 *Modeling groundwater flow and contaminant transport*. New York, NY: Springer.
3. Huppert H, Neufeld J. 2014 The fluid mechanics of carbon dioxide sequestration. *Annu. Rev. Fluid Mech.* **46**, 255–272. (doi:10.1146/annurev-fluid-011212-140627)
4. Woods A. 2015 *Flow in porous rocks*. Cambridge, UK: Cambridge University Press.
5. Huppert H, Woods A. 1995 Gravity-driven flows in porous layers. *J. Fluid Mech.* **292**, 55–69. (doi:10.1017/S0022112095001431)
6. Hesse M, Orr F, Tchelepi H. 2008 Gravity currents with residual trapping. *J. Fluid Mech.* **611**, 35–60. (doi:10.1017/S002211200800219X)
7. Golding M, Huppert H, Neufeld J. 2017 Two-phase gravity currents resulting from the release of a fixed volume of fluid in a porous medium. *J. Fluid Mech.* **832**, 550–577. (doi:10.1017/jfm.2017.437)
8. MacMinn C, Szulczewski M, Juanes R. 2011 CO_2 migration in saline aquifers. Part 2. Capillary and solubility trapping. *J. Fluid Mech.* **688**, 321–351. (doi:10.1017/jfm.2011.379)
9. Barenblatt G. 1952 On some unsteady motions of a fluid and a gas in a porous medium. *Prikl. Mat. Makh.* **16**, 67–78.
10. Kochina I, Mikhailov N, Filinov M. 1983 Groundwater mound damping. *Int. J. Eng. Sci.* **21**, 413–421. (doi:10.1016/0020-7225(83)90124-6)
11. Hesse M, Tchelepi H, Cantwel B, Orr F. 2007 Gravity currents in horizontal porous layers: transition from early to late self-similarity. *J. Fluid Mech.* **577**, 363–383. (doi:10.1017/S0022112007004685)
12. Ball T, Huppert H, Lister J, Neufeld J. 2017 The relaxation time for viscous and porous gravity currents following a change in flux. *J. Fluid Mech.* **821**, 330–342. (doi:10.1017/jfm.2017.243)
13. Zheng Z. 2023 The radial slump of a gravity current in a confined porous layer. *Proc. R. Soc. A.* **479**, 20220696. (doi:10.1098/rspa.2022.0696)
14. Cheng P, Bestehorn M, Firoozabadi A. 2012 Effect of permeability anisotropy on buoyancy-driven flow for CO_2 sequestration in saline aquifers. *Water Resour. Res.* **48**, 000. (doi:10.1029/2011WR011799)
15. Green C, Ennis-King J. 2014 Steady dissolution rate due to convective mixing in anisotropic porous media. *Adv. Water Resour.* **73**, 65–73. (doi:10.1016/j.advwatres.2014.07.002)
16. De Paoli M, Zonta F, Soldati A. 2017 Dissolution in anisotropic porous media: modelling convection regimes from onset to shutdown. *Phys. Fluids* **29**, 026601. (doi:10.1063/1.4975393)
17. Jackson S, Krevor S. 2020 Small-scale capillary heterogeneity linked to rapid plume migration during CO_2 storage. *Geophys. Res. Lett.* **47**, e2020GL088616. (doi:10.1029/2020GL088616)
18. Benham G, Neufeld J, Woods A. 2022 Axisymmetric gravity currents in anisotropic porous media. *J. Fluid Mech.* **952**, A23. (doi:10.1017/jfm.2022.922)
19. Krevor S, Blunt M, Benson S, Pentland C, Reynolds C, Al-Menhali A, Niu B. 2015 Capillary trapping for geologic carbon dioxide storage–From pore scale physics to field scale implications. *Int. J. Greenh. Gas Con.* **40**, 221–237. (doi:10.1016/j.ijggc.2015.04.006)
20. Mondal R, Benham G, Mondal S, Christodoulides P, Neokleous N, Kaouri K. 2019 Modelling and optimisation of water management in sloping coastal aquifers with seepage, extraction and recharge. *J. Hydrol.* **571**, 471–484. (doi:10.1016/j.jhydrol.2019.01.060)
21. Corbett P, Jensen J. 1992 Variation of reservoir statistics according to sample spacing and measurement type for some intervals in the Lower Brent Group. *Log Anal.* **33**.
22. Soltanian M, Amooie M, Dai Z, Cole D, Moortgat J. 2016 Critical dynamics of gravito-convective mixing in geological carbon sequestration. *Sci. Rep.* **6**, 1–13. (doi:10.1038/srep35921)
23. Pegler S, Huppert H, Neufeld J. 2014 Fluid injection into a confined porous layer. *J. Fluid Mech.* **745**, 592–620. (doi:10.1017/jfm.2014.76)

24. Gilmore K, Sahu C, Benham G, Neufeld J, Bickle M. 2022 Leakage dynamics of fault zones: experimental and analytical study with application to CO_2 storage. *J. Fluid Mech.* **931**, 2021970. (doi:10.1017/jfm.2021.970)
25. Benham G. 2023 The near-field shape and stability of a porous plume. *J. Fluid Mech.* **955**, A13. (doi:10.1017/jfm.2022.1068)
26. Van Dyke M. 1975 Perturbation methods in fluid mechanics. *NASA STI/Recon Technical Rep. A* **75**, 46926.
27. Lyle S, Huppert H, Hallworth M, Bickle M, Chadwick A. 2005 Axisymmetric gravity currents in a porous medium. *J. Fluid Mech.* **543**, 293–302. (doi:10.1017/S0022112005006713)
28. Sahu C, Flynn M. 2015 Filling box flows in porous media. *J. Fluid Mech.* **782**, 455–478. (doi:10.1017/jfm.2015.555)
29. Benham G, Bickle M, Neufeld J. 2021 Two-phase gravity currents in layered porous media. *J. Fluid Mech.* **922**, A7. (doi:10.1017/jfm.2021.523)
30. Benham G, Bickle M, Neufeld J. 2021 Upscaling multiphase viscous-to-capillary transitions in heterogeneous porous media. *J. Fluid Mech.* **911**, A59. (doi:10.1017/jfm.2020.1134)
31. Neufeld J, Huppert H. 2009 Modelling carbon dioxide sequestration in layered strata. *J. Fluid Mech.* **625**, 353–370. (doi:10.1017/S0022112008005703)
32. Hewitt D. 2022 Evolution of convection in a layered porous medium. *J. Fluid Mech.* **941**, 2022335. (doi:10.1017/jfm.2022.335)
33. Harris C, Jackson S, Benham G, Krevor S, Muggeridge A. 2021 The impact of heterogeneity on the capillary trapping of CO_2 in the Captain Sandstone. *Int. J. Greenh. Gas Con.* **112**, 103511. (doi:10.1016/j.ijggc.2021.103511)
34. Saffman P, Taylor G. 1958 The penetration of a fluid into a porous medium or Hele-Shaw cell containing a more viscous liquid. *Proc. R. Soc. Lond. A* **245**, 312–329. (doi:10.1098/rspa.1958.0085)
35. Köllner T, Meredith A, Nokes R, Meiburg E. 2020 Gravity currents over fixed beds of monodisperse spheres. *J. Fluid Mech.* **901**, A32. (doi:10.1017/jfm.2020.550)
36. Benham GP. 2023 Anisotropy distorts the spreading of a fixed volume porous gravity current. Figshare. (doi:10.6084/m9.figshare.c.6922121)